nature materials

SUPPLEMENTARY INFORMATION

https://doi.org/10.1038/s41563-020-0708-6

In the format provided by the authors and unedited.

Correlated electronic phases in twisted bilayer transition metal dichalcogenides

Lei Wang[1,2,11], En-Min Shih[2,11], Augusto Ghiotto[2,11], Lede Xian[3], Daniel A. Rhodes[4], Cheng Tan[4,5], Martin Claassen[6], Dante M. Kennes[3,7], Yusong Bai[8], Bumho Kim[4], Kenji Watanabe[9], Takashi Taniguchi[9], Xiaoyang Zhu[8], James Hone[4], Angel Rubio[3,6,10] ✉, Abhay N. Pasupathy[2] ✉ and Cory R. Dean[2] ✉

[1]National Laboratory of Solid-State Microstructures, School of Physics and Collaborative Innovation Center of Advanced Microstructures, Nanjing University, Nanjing, China. [2]Department of Physics, Columbia University, New York, NY, USA. [3]Max Planck Institute for the Structure and Dynamics of Matter, Hamburg, Germany. [4]Department of Mechanical Engineering, Columbia University, New York, NY, USA. [5]Department of Electrical Engineering, Columbia University, New York, NY, USA. [6]Center for Computational Quantum Physics, Flatiron Institute, New York, NY, USA. [7]Institut für Theorie der Statistischen Physik RWTH Aachen University and JARA-Fundamentals of Future Information Technology, Aachen, Germany. [8]Department of Chemistry, Columbia University, New York, NY, USA. [9]National Institute for Materials Science, Tsukuba, Ibaraki, Japan. [10]Nano-Bio Spectroscopy Group, Departamento de Fisica de Materiales, Universidad del País Vasco, San Sebastian, Spain. [11]These authors contributed equally: Lei Wang, En-Min Shih and Augusto Ghiotto. ✉e-mail: angel.rubio@mpsd.mpg.de; apn2108@columbia.edu; cdean@phys.columbia.edu

Supplementary Information: Correlated electronic phases in twisted bilayer transition metal dichalcogenides

Lei Wang[1,2 †], En-Min Shih[2 †], Augusto Ghiotto[2 †], Lede Xian[3], Daniel A. Rhodes[4], Cheng Tan[4,5], Martin Claassen[6], Dante M. Kennes[3,7], Yusong Bai[8], Bumho Kim[4], Kenji Watanabe[9], Takashi Taniguchi[9], Xiaoyang Zhu[8], James Hone[4], Angel Rubio[3,6,10 *], Abhay Pasupathy[2 *], and Cory R. Dean[2*]

[1] *National Laboratory of Solid-State Microstructures, School of Physics, Nanjing University, Nanjing, 210093, China*

[2] *Department of Physics, Columbia University, New York, NY 10027, USA*

[3] *Max Planck Institute for the Structure and Dynamics of Matter, Luruper Chaussee 149, 22761 Hamburg, Germany*

[4] *Department of Mechanical Engineering, Columbia University, New York, NY 10027, USA*

[5] *Department of Electrical Engineering, Columbia University, New York, NY 10027, USA*

[6] *Center for Computational Quantum Physics, Flatiron Institute, New York, NY 10010, USA*

[7] *Institut für Theorie der Statistischen Physik, RWTH Aachen University, 52056 Aachen, Germany and JARA-Fundamentals of Future Information Technology, 52056 Aachen, Germany*

[8] *Department of Chemistry, Columbia University, New York, NY 10027, USA*

[9] *National Institute for Materials Science, Namiki 1-1, Tsukuba, Ibaraki 305-0044, Japan*

[10] *Nano-Bio Spectroscopy Group, Departamento de Fisica de Materiales, Universidad del País Vasco, 20018 San Sebastian, Spain*

[†] *These authors contributed equally to this work. and*

[*] *Corresponding authors, Email: cdean@phys.columbia.edu, apn2108@columbia.edu, angel.rubio@mpsd.mpg.de*

(Dated: April 11, 2020)

BAND STRUCTURE CALCULATION

In order to study the electronic properties of twisted bilayer WSe_2, we perform first principle calculations based on density functional theory (DFT). We extend and complement these results with insights obtained from tight-binding calculations. The DFT calculations are performed with the Vienna Ab initio Simulation Package (VASP) [1]. Plane-wave basis sets are employed with an energy cutoff of $550eV$. The projector augmented wave method (PAW) [2] is used to construct the pseudopotentials felt by the valence electrons. The exchange-correlation functionals are treated within the generalized gradient approximations (GGA). For systems with twist angle larger than 5.1 degrees, a 3x3x1 Gamma-centered k-grid is used, and for the other, larger systems (at smaller angle), a Gamma-only k-grid is employed. All atoms are relaxed until the force on each atom is less than $0.01eV/$Å. Van der Waals interactions are included using the method of Tkatchenko and Scheffler [3] during the relaxation. We employ an optimized lattice constant of 3.30Å for a 1x1 WSe_2 bilayer with Bernal stacking. Spin-orbit interactions are considered in all the band structure calculations. We perform extensive DFT calculations at zero displacement field, for several angles as well as for several displacement fields at one angle of 5.08 degree. This allows us to obtain a complete picture. Subsequently we fit the top of the valence band calculated by DFT using tight-binding (TB) models, which allows us to efficiently obtain results also for different displacement fields from those (see Fig. 19). Using this TB approach yields a dramatic speed up and allows to calculate the density of states using a high resolution in momentum space, which is necessary to track the van-Hove singularity accurately (see main text). The TB calculations are based on a twisted bilayer honeycomb lattice with one orbital for each lattice site. The lattice constants are the same as those used in the DFT calculations and the interlayer separation is set to be 6.53Å. We employed a hopping term that only depends on the separation between the two sites, similar to the one used for twisted bilayer graphene [4, 5]. The onsite energy difference between the two sublattices in each layer is set to be $1.23eV$. We use a Gaussian smearing of $2meV$ in the calculation of density of states with the TB method and a k-grid as large as 40x40x1 in the supercell Brillouin zone to ensure the calculation is converged.

LOW ENERGY MODEL AND MEAN FIELD THEORY CALCULATION OF INTERACTIONS

In order to study the effects of correlations in the twisted bilayer, we commence by devising an effective low-energy tight-binding model of the moiré band structure. In contrast to the effective twisted WSe_2 tight-binding model utilized in the ab initio calculations detailed above to extract the displacement field dependence, we construct here a symmetry-adapted spin-orbit coupled single-orbital triangular-lattice model of solely the highest two moiré minibands.

Compared to the case of twisted bilayer graphene near the magic angle, a low-energy description of the partially-filled moiré band need only take into account time-reversal symmetry as well as the C_3 rotation sym-

metry of the lattice which is preserved in the twisted bilayer. Furthermore, ab initio calculations of the spin polarization of the bands along a high symmetry cut at a finite displacement field indicate that the spin-flip contributions to spin-orbit coupling is negligible. We therefore start from a third-nearest-neighbor single-orbital tight-binding model on the triangular lattice with solely spin-conserving spin-orbit coupling, with dispersions

$$\epsilon_{\sigma=\uparrow,\downarrow}(\mathbf{k}) = \epsilon_0 + t(\mathbf{k}) + \sigma\lambda(\mathbf{k}) \tag{1}$$

where ϵ_0 is a constant energy shift, $t(\mathbf{k})$ are hopping matrix elements, with

D	ϵ_0	t_1	t_2	t_3	t_4	t_5	t_6
0.0	-0.6818	-0.0155	-0.0034	0.0001	-0.0011	-0.0003	-0.0003
0.005	-0.6819	-0.0156	-0.0033	0.0002	-0.0012	-0.0003	-0.0003
0.01	-0.6818	-0.0155	-0.0033	0	-0.0010	-0.0003	-0.0003
0.015	-0.6801	-0.0153	-0.0031	-0.0002	-0.0008	-0.0003	-0.0003
0.02	-0.6796	-0.0153	-0.0029	-0.0005	-0.0007	-0.0003	-0.0003
0.025	-0.6775	-0.0150	-0.0027	-0.0006	-0.0006	-0.0004	-0.0004
0.03	-0.6757	-0.0148	-0.0024	-0.0009	-0.0004	-0.0005	-0.0005
0.035	-0.6742	-0.0145	-0.0022	-0.0012	-0.0003	-0.0006	-0.0006
0.04	-0.6726	-0.0142	-0.0019	-0.0015	-0.0002	-0.0007	-0.0007
0.045	-0.6709	-0.0139	-0.0017	-0.0018	0	-0.0008	-0.0008
0.05	-0.6689	-0.0136	-0.0014	-0.0021	0	-0.0009	-0.0009
0.06	-0.6649	-0.0129	-0.0009	-0.0027	0.0003	-0.0011	-0.0011
0.07	-0.6607	-0.0123	-0.0005	-0.0033	0.0004	-0.0012	-0.0012
0.08	-0.6564	-0.0118	-0.0002	-0.0039	0.0003	-0.0012	-0.0012
0.09	-0.6520	-0.0114	0	-0.0044	0.0002	-0.0011	-0.0011

TABLE I. Tight-binding parameters of the low-energy triangular-lattice moiré miniband model of equation (1), as a function of displacement field.

$$\begin{aligned} t(\mathbf{k}) = {} & t_1\left[\cos(k_1)+\cos(k_2)+\cos(k_2-k_1)-3\right] \\ & + t_2\left[\cos(2k_1)+\cos(2k_2)+\cos(2k_2-2k_1)-3\right] \\ & + t_3[\cos(k_1+k_2)+\cos(2k_1-k_2)+\cos(k_1-2k_2) \\ & - 3] \\ & + t_4\left[\cos(3k_1)+\cos(3k_2)+\cos(3k_2-3k_1)-3\right] \\ & + t_5[\cos(k_1-3k_2)+\cos(3k_1-2k_2)+\cos(2k_1+k_2) \\ & - 3] \\ & + t_6[\cos(2k_1-3k_2)+\cos(3k_1-k_2)+\cos(k_1+2k_2) \\ & - 3] \end{aligned} \tag{2}$$

where $k_i = \mathbf{a}_i \cdot \mathbf{k}$, and $\lambda(\mathbf{k})$ models spin-conserving spin-orbit coupling with

D	λ_1	λ_2	λ_3	λ_4	λ_5	λ_6
0.0	0.0006	0.0009	-0.0018	0.0002	-0.0010	-0.0002
0.005	0.0006	0.0009	-0.0018	0.0002	-0.0010	-0.0002
0.01	0.0025	0.0007	-0.0019	0.0003	-0.0007	-0.0007
0.015	0.0038	0.0011	-0.0017	0.0004	-0.0006	-0.0005
0.02	0.0051	0.0014	-0.0016	0.0006	-0.0006	-0.0005
0.025	0.0063	0.0018	-0.0015	0.0007	-0.0005	-0.0005
0.03	0.0074	0.0021	-0.0014	0.0007	-0.0004	-0.0005
0.035	0.0085	0.0025	-0.0014	0.0009	-0.0003	-0.0005
0.04	0.0095	0.0028	-0.0013	0.001	-0.0001	-0.0006
0.045	0.0106	0.0031	-0.0013	0.0011	-0.0001	-0.0006
0.05	0.0116	0.0033	-0.0012	0.0011	0	-0.0006
0.06	0.0133	0.0035	0.0012	0.001	0.0007	-0.0001
0.07	0.0148	0.0034	-0.0011	0.0007	0.0003	-0.0008
0.08	0.0161	0.0034	-0.0011	0.0004	0.0004	-0.0010
0.09	0.0172	0.0034	-0.0011	0.0003	0.0006	-0.0011

TABLE II. Tight-binding parameters of the low-energy triangular-lattice moiré miniband model of equation (1), as a function of displacement field.

$$\begin{aligned} \lambda(\mathbf{k}) = {} & \lambda_1\left[\sin(k_1)-\sin(k_2)-\sin(k_1-k_2)\right] \\ & + \lambda_2\left[\sin(2k_1)-\sin(2k_2)-\sin(2k_1-2k_2)\right] \\ & + \lambda_3\left[\sin(k_1-2k_2)-\sin(2k_1-k_2)+\sin(k_1+k_2)\right] \\ & + \lambda_4\left[\sin(3k_1)-\sin(3k_2)-\sin(3k_1-3k_2)\right] \\ & + \lambda_5\left[\sin(k_1-3k_2)-\sin(3k_1-2k_2)+\sin(2k_1+k_2)\right] \\ & + \lambda_6\left[\sin(2k_1-3k_2)-\sin(3k_1-k_2)+\sin(k_1+2k_2)\right] \end{aligned} \tag{3}$$

The tight-binding parameters t_n, λ_n are determined by fitting to the ab initio band structure.

To treat the correlated insulating state, we consider a minimal model with a local Hubbard interaction

$$\hat{H} = \sum_{\mathbf{k}\sigma} \epsilon_\sigma(\mathbf{k})\ \hat{c}^\dagger_{\mathbf{k}\sigma}\hat{c}_{\mathbf{k}\sigma} + U\sum_{\mathbf{k}\mathbf{k}'\mathbf{q}} \hat{c}^\dagger_{\mathbf{k}+\mathbf{q},\uparrow}\hat{c}^\dagger_{\mathbf{k}'-\mathbf{q},\downarrow}\hat{c}_{\mathbf{k}'\downarrow}\hat{c}_{\mathbf{k}\uparrow} \tag{4}$$

and study the behavior as a function of the displacement field dependence of the tight-binding parameters.

While the strength of the effective screened Coulomb repulsion as well as its dependence on the displacement field cannot be reliably determined from ab initio calculations of the moiré supercell, an order-of-magnitude estimate readily follows from the experimental observations. The dependence of the insulating state on the displacement field rules out the strong coupling limit with $U > W$ with $W \sim 100meV$ the non-interacting bandwidth of (1). In this scenario, the opening of a charge gap is associated with an energy/temperature scale $\propto U$ that remains insensitive to weak displacement-field perturbations of the band structure and spin-orbit coupling matrix elements. Conversely, at infinitesimal coupling $U \ll W$ the insulating state would be determined by

the location of the van Hove singularity and hence be expected to shift to filling fractions away from half filling as a function of displacement field, which is not observed in experiment. These considerations place the interaction strength in an intermediate coupling regime.

While the intermediate-coupling regime on a frustrated lattice poses significant challenges to a quantitative theoretical treatment, we instead qualitatively model the trend of the insulating phase as a function of displacement field via a mean field theory calculation as a function of the displacement field dependent tight-binding parameters. In mean field theory, the appearance of a charge gap is tied to the formation of magnetic or charge order. To this end, in single-orbital triangular lattice Mott insulators with short-ranged effective spin-exchange interactions, the ground state has previously been shown to be a $\sqrt{3} \times \sqrt{3}$ Néel state. We therefore adopt a Néel state with ordering vector $\mathbf{q} = (4\pi/3, 0)$ for the purpose of a mean field theory calculation and furthermore pin the chemical potential as a function of displacement field to enforce half filling of the moiré band as expected for an intermediate coupling regime. We emphasize that the choice of magnetic order, while motivated by previous studies of triangular-lattice Mott insulators, is in principle arbitrary – since Fermi surface nesting is largely absent in the moiré miniband model for the displacement fields studied here, the enhancement and suppression of the correlated state in weak coupling follows solely from the shifting of the van Hove singularity across the Fermi surface as a function of displacement field and can in principle be reproduced via other and possibly incommensurate magnetic orders.

Under these assumptions, we calculate the density of states on a 100×100 momentum-space grid to determine the half-filling point, and solve the mean field self-consistency equations which are parameterized by the displacement field dependence. As a function of interaction strength, the critical temperature, and equivalently the gap size of the insulating state, develop a dome-like shape at weak interactions, with a peak at the displacement field value at which the van Hove singularity lies on the Fermi surface. Upon increasing U, the dome saturates to a plateau that spans from zero displacement field up to a critical value, beyond which the system becomes metallic. The experimental observation of the displacement field dependent metal insulator transition is therefore well-modelled by choosing a Hubbard interaction $\sim 0.5 - 0.7meV$.

[1] G. Kresse and J. Hafner, Phys. Rev. B **47**, 558 (1993).
[2] P. E. Blöchl, Phys. Rev. B **50**, 17953 (1994).
[3] A. Tkatchenko and M. Scheffler, Phys. Rev. Lett. **102**, 073005 (2009).
[4] G. Trambly de Laissardière, D. Mayou, and L. Magaud, Nano Letters **10**, 804 (2010).
[5] G. Trambly de Laissardière, D. Mayou, and L. Magaud, Physical Review B **86**, 125413 (2012).
[6] A. Laturia and M. L. V. D. Put, npj 2D Materials and Applications , 1 (2018).
[7] Y. Cao, V. Fatemi, A. Demir, S. Fang, S. L. Tomarken, J. Y. Luo, J. D. Sanchez-Yamagishi, K. Watanabe, T. Taniguchi, E. Kaxiras, R. C. Ashoori, and P. Jarillo-Herrero, Nature **556**, 80 (2018).

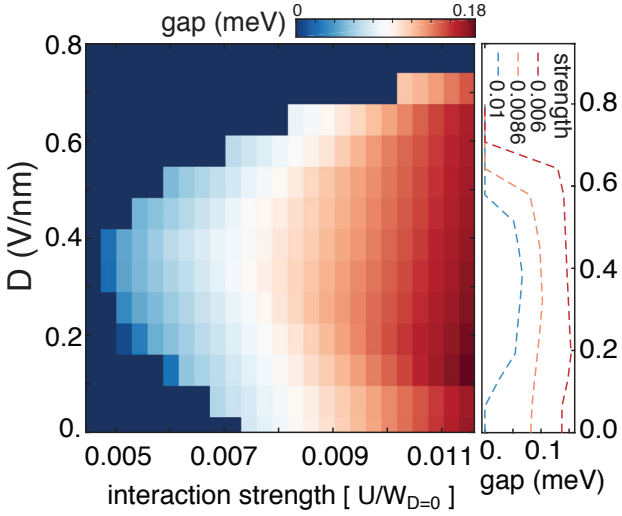

FIG. 1. **Mean-field calculation. Left:** Gap size versus displacement field and assumed strength of the Coulomb interaction in a false color plot. **Right:** Line cuts for the gap size as a function of displacement field for a select interaction strengths. At relatively weak interaction strength there is a pronounced dome structure (in agreement with the experimental reports) that saturates as the interaction is increased.

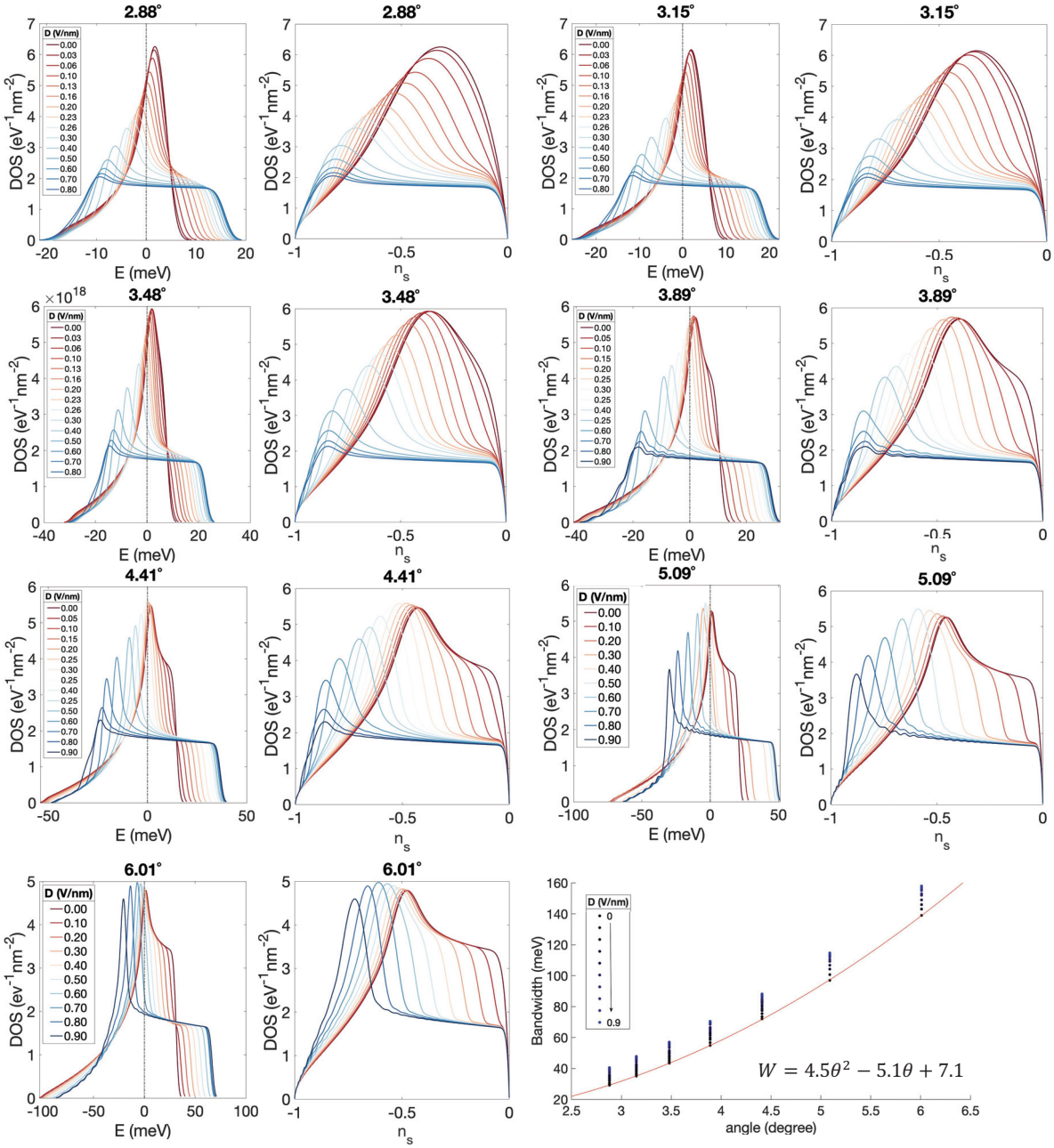

FIG. 2. **Calculated density of states and bandwidths.** Density of states of the top moiré valence band versus energy or relative filling for different twist angles and displacement fields. Energy is offset to half-filling of the moiré unit cell. Bottom right: summary plot of the bandwidth of the top valence band versus twist angle for different D fields. A quadratic fit to the $D = 0$ bandwidths is also shown.

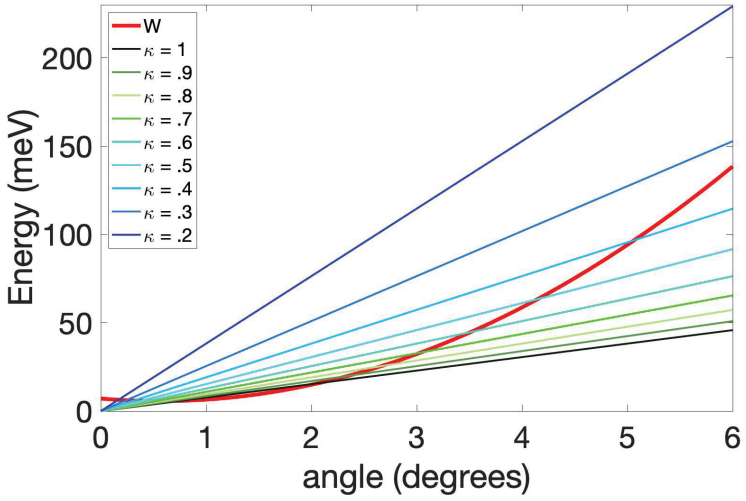

FIG. 3. **Bandwidth versus Coulomb interaction.** Considering the Coulomb interaction energy to be $U = e^2/4\pi\epsilon_0\epsilon_r\kappa L$, where $\epsilon_r \sim 10$ is the effective in-plane dielectric screening in the bilayer [6], L is the moiré wavelength and κ factors are uncertainties in the ϵ_r and the separation of wavefunctions in regards to L [7].

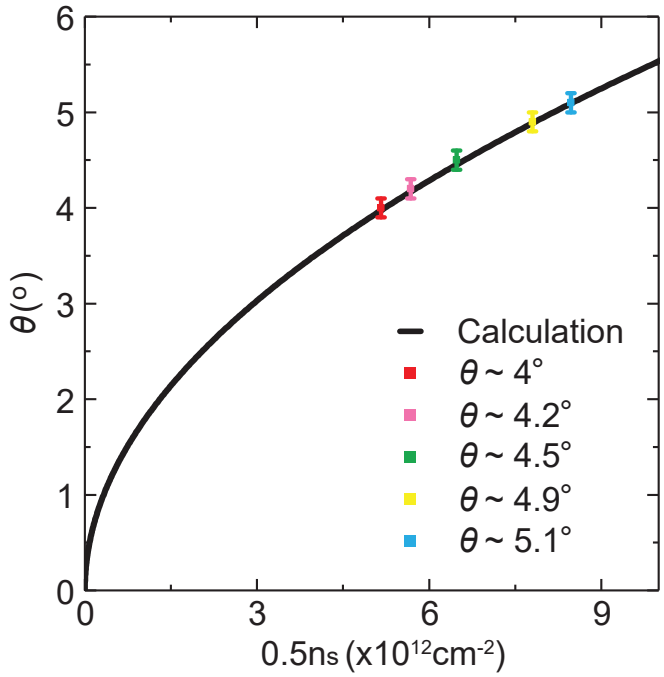

FIG. 4. **Twist angle versus half-filling density.** Calculated line (black) obtained from $n_s = \frac{2}{\frac{\sqrt{3}}{2}\lambda^2}$ and $\lambda = \frac{a}{\sqrt{2(1-cos\theta)}}$, where $a = 0.328$ nm is the lattice constant of WSe_2 and full-filling (n_s) assumes two holes per moiré unit cell, consistent with Landau level degeneracies. Twist angle obtained from Landau fans versus half-filling density is also plotted.

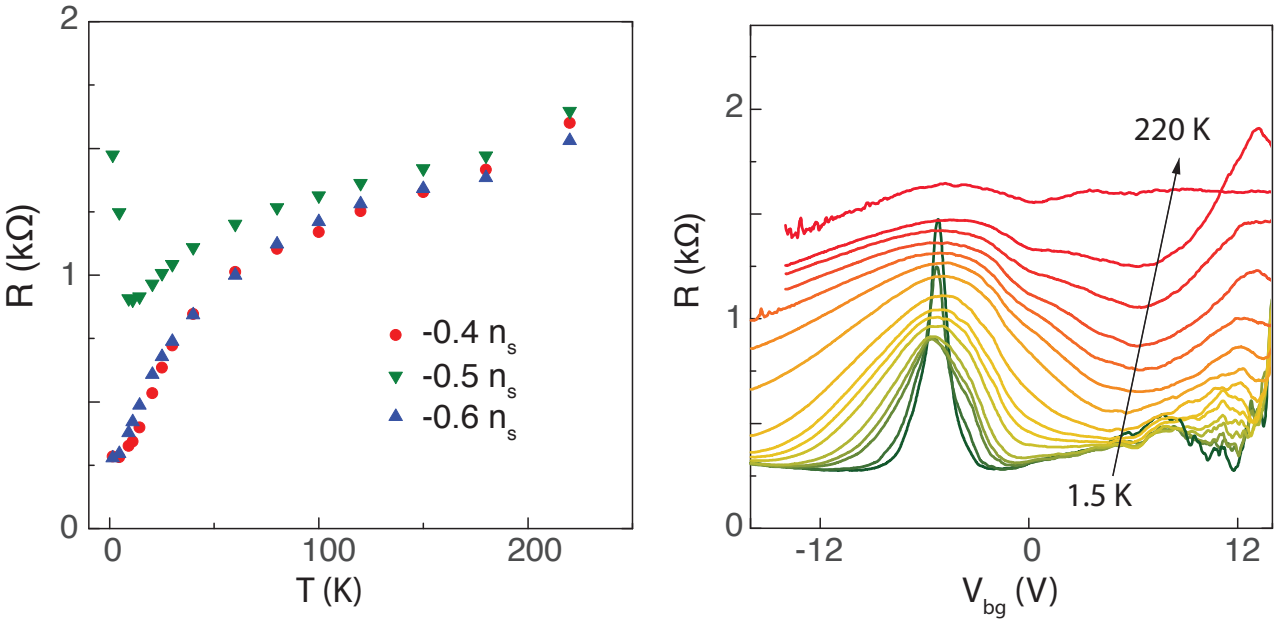

FIG. 5. **Temperature dependence of the Mott state for the 4.5° sample. Left:** Resistance versus temperature for densities at half-filling and its neighborhood. An insulating state forms at half-filling and there is a steeper drop in resistance in the neighboring densities. **Right:** Resistance versus back gate voltage from 1.5K to 220K for the same sample.

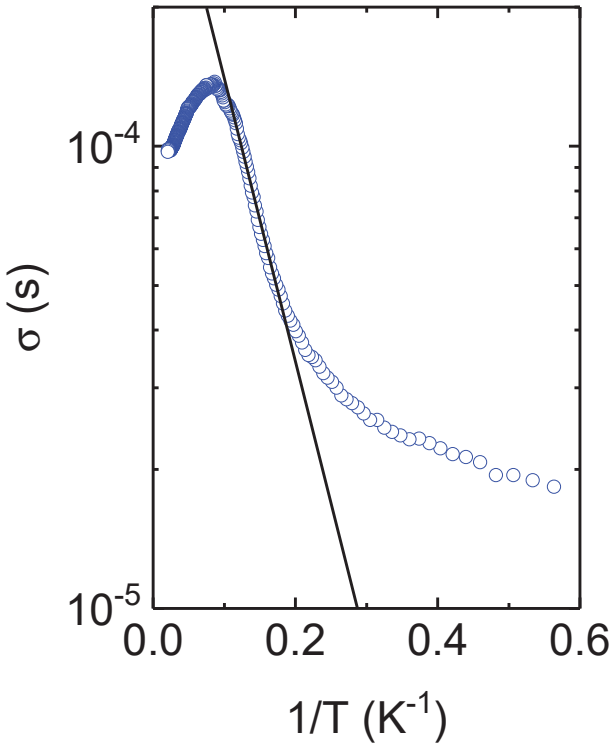

FIG. 6. **Arrhenius plot of correlated insulating state for 4.2 ° device (shown in main text Fig. 1e).** Logarithm of conductance σ versus $1/T$ at $D = 0.15$ V/nm. The linear region is fit to $\sigma \sim e^{-\frac{\Delta}{2k_B T}}$ and we find $\Delta \sim 2.4 \pm 0.1$meV.

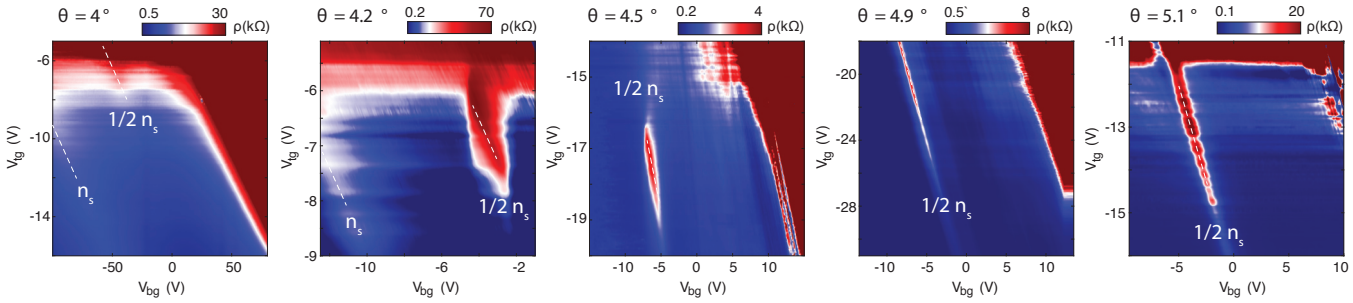

FIG. 7. **Resistance maps as a function of top and bottom gates for 4°, 4.2°, 4.5°, 4.9° and 5.1° twist angle.**

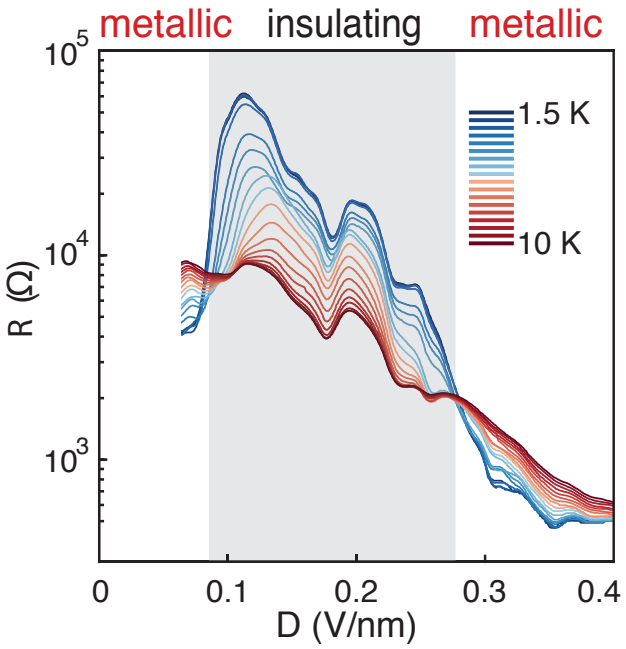

FIG. 8. **Gate tunable metal-to-insulator transition in a 4.2° device.** Resistivity curves at half-filling versus displacement field from 1.5K to 10K. Two separatrices of metallic and insulating regions are observed at $D = 0.08$ V/nm and 0.27 V/nm.

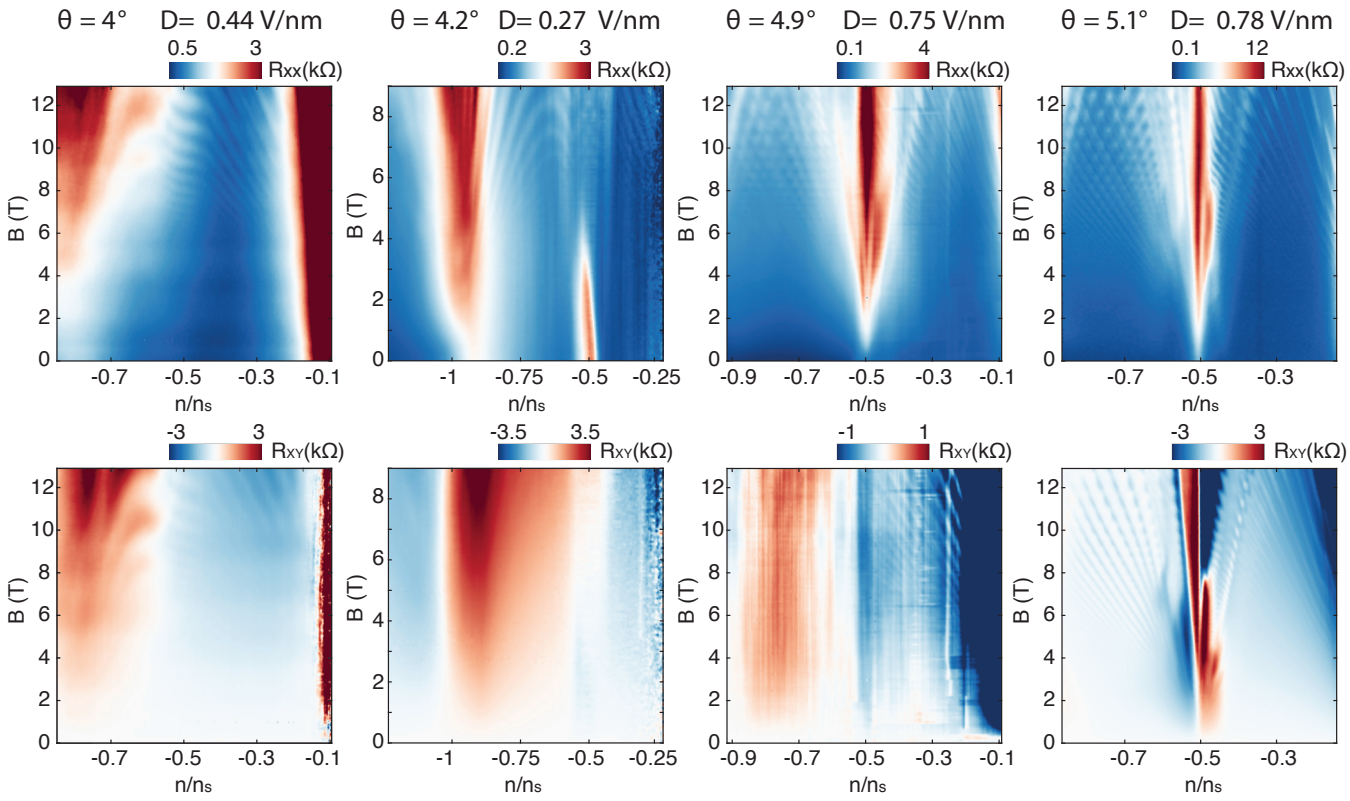

FIG. 9. **Magnetotransport for for 4°, 4.2°, 4.9°and 5.1° devices.** Landau fan tracing to the full-filling is shown in all samples. Sign-flip in Hall resistance associated with the insulating peak in longitudinal resistance is also observed.

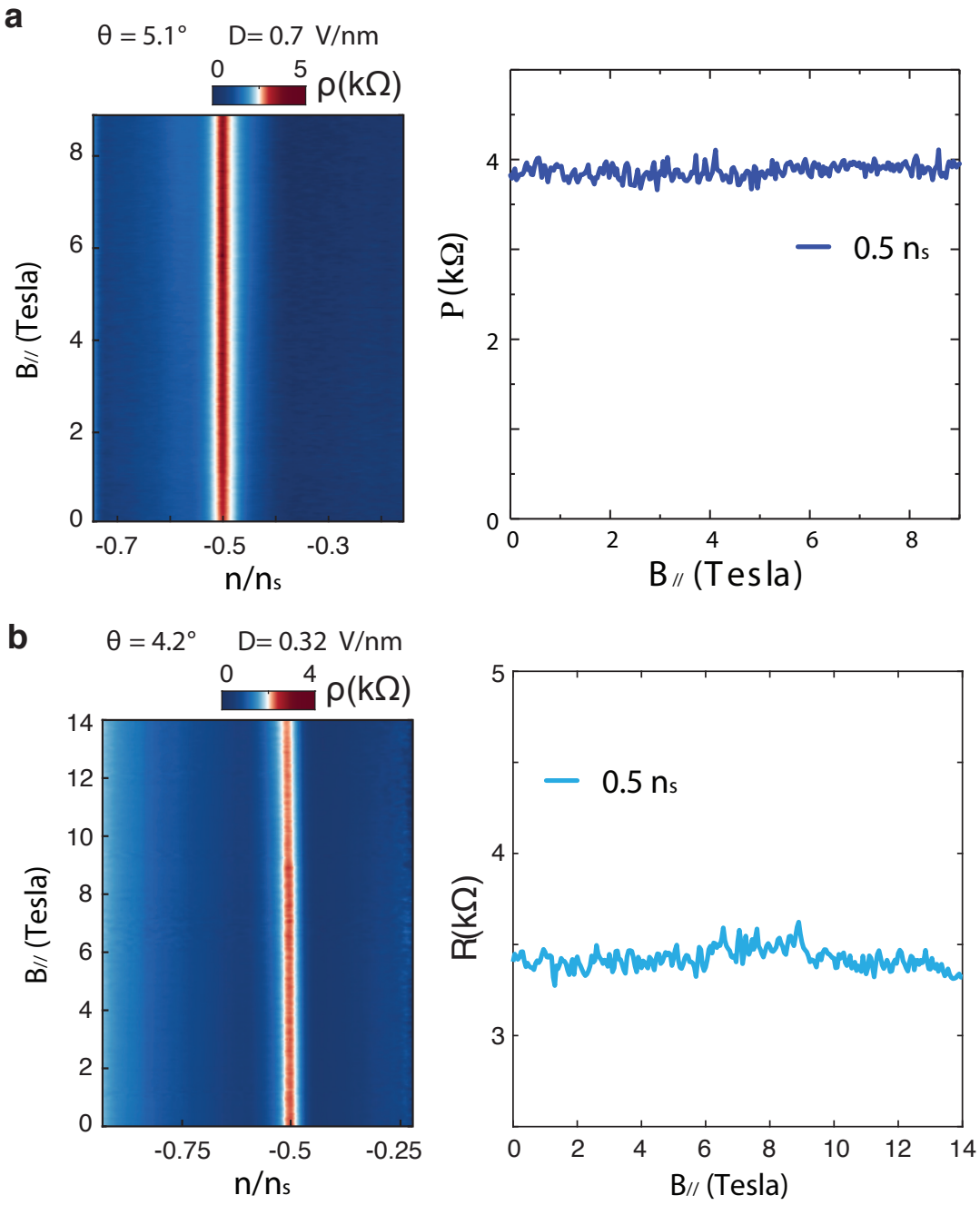

FIG. 10. **Parallel B field dependence of correlated insulating state. a,** 4.2° device. Left: resistance versus parallel B field and band-filling. Right: line cut of resistance versus parallel B field at half-filling. **b,** 5.1 ° device. Left: resistance versus parallel B field and band-filling. Right: line cut of resistance versus parallel B field at half-filling.

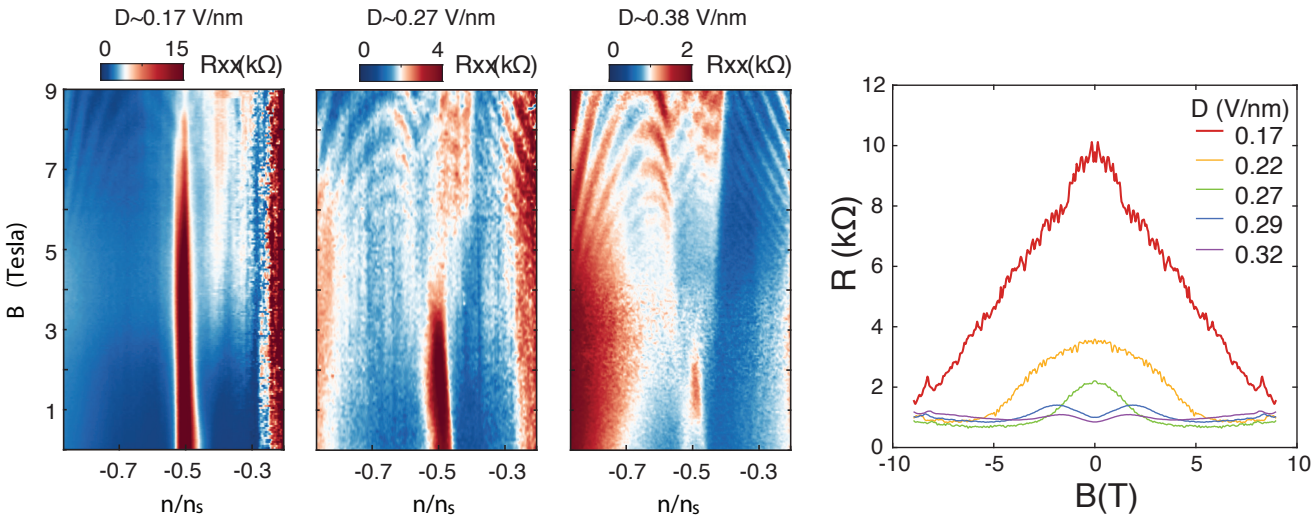

FIG. 11. **Perpendicular B-field effect on the correlated insulator for 4.2° device. Left:** Effect of perpendicular magnetic field on the correlated insulator gap for different displacement field values. Note that the gap is re-entrant for $D = 0.38$ V/nm, a region in which the device exhibits metallic behaviour at half-filling when B=0. **Right:** Resistance at half filling versus magnetic field for various displacement fields.

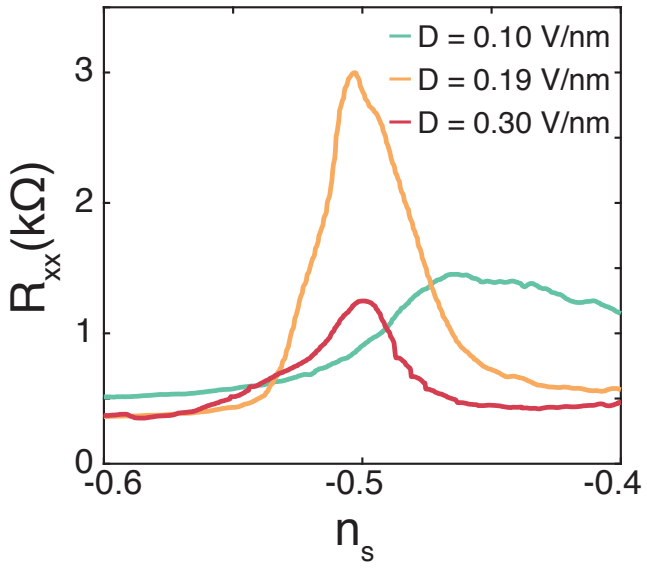

FIG. 12. $\mathbf{R}_{xx}$ **corresponding to the** $\mathbf{R}_{xy}$ **in main text Fig. 2c.**

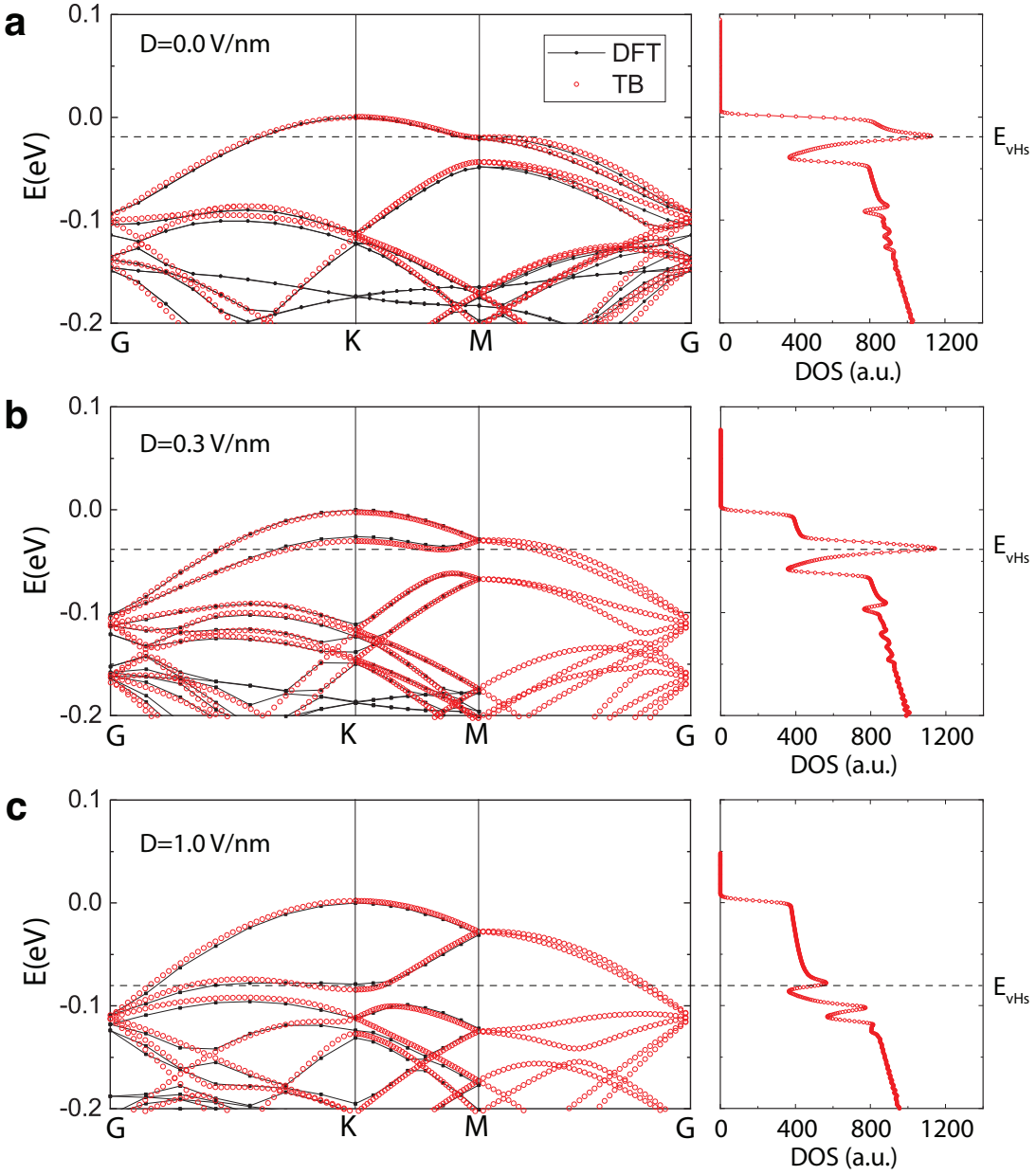

FIG. 13. **Evolution of the band structure and DOS of twisted bilayer WSe_2 5.08° with increasing displacement field.** The DFT results and the corresponding TB fits are represented by black solid lines and red circles, respectively. The positions of the van Hove singularity are indicated with horizontal dash lines.

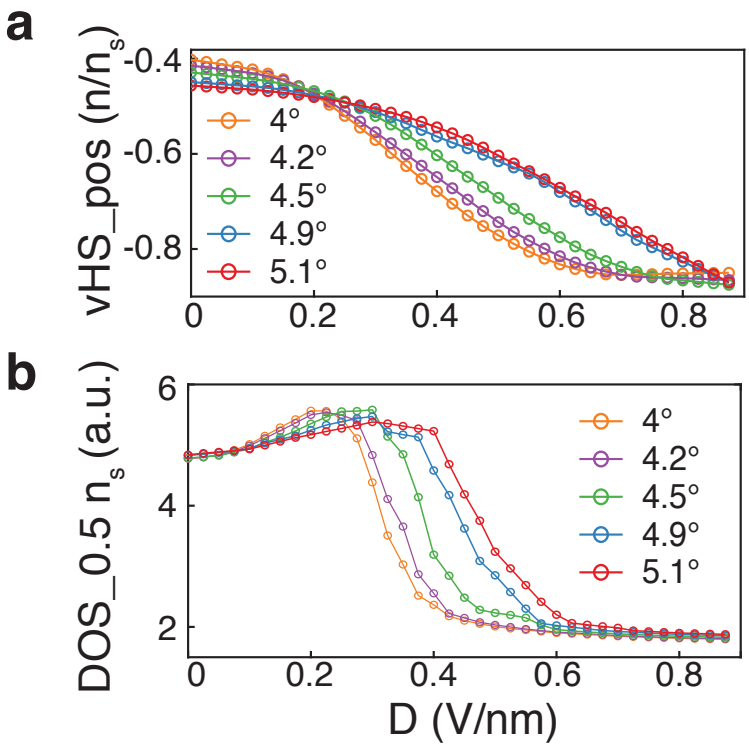

FIG. 14. **Dependence of vHS position and DOS at half filling as a function of displacement field D at different twist angles. a,** vHS moves to higher filling with increasing D. The rate of change is larger for smaller twist angle. **b,** The maximum DOS at half-filling is at finite D and moves to larger D at larger angle.

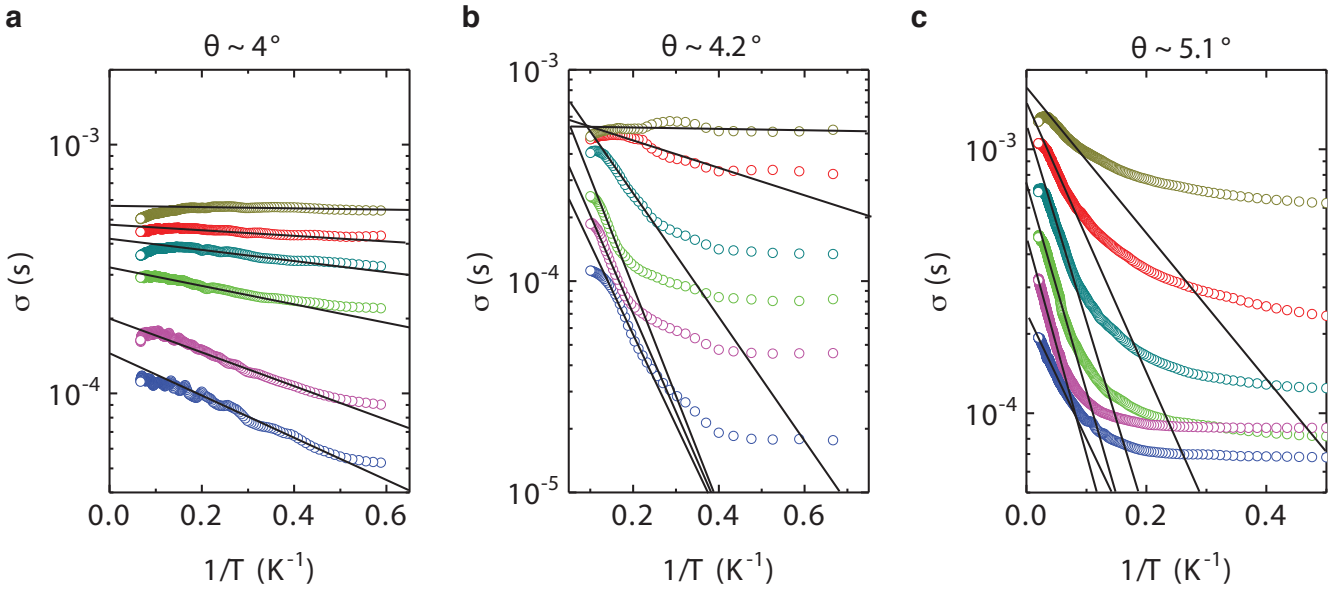

FIG. 15. **Arrhenius plot of correlated insulating state for 4°, 4.2° and 5° devices.** Logarithm of conductance σ versus $1/T$ at different displacement fields. The linear region is fit to $\sigma \sim e^{-\frac{\Delta}{2k_BT}}$. **a,** Legend: blue ($D = 0.06$ V/nm, $\Delta \sim 0.34$ meV); purple ($D = 0.08$ V/nm, $\Delta \sim 0.23$ meV); green ($D = 0.11$ V/nm, $\Delta \sim 0.15$ meV); cyan ($D = 0.13$ V/nm, $\Delta \sim 0.07$ meV); red ($D = 0.15$ V/nm, $\Delta \sim 0.04$ meV); yellow ($D = 0.16$ V/nm, $\Delta \sim 0.0$ meV). **b,** Legend: blue ($D = 0.11$ V/nm, $\Delta \sim 1.7$ meV); purple ($D = 0.12$ V/nm, $\Delta \sim 1.9$ meV); green ($D = 0.15$ V/nm, $\Delta \sim 2.2$ meV); cyan ($D = 0.23$ V/nm, $\Delta \sim 1.2$ meV); red ($D = 0.27$ V/nm, $\Delta \sim 0.12$ meV); yellow ($D = 0.28$ V/nm, $\Delta \sim 0.0$ meV). **c,** Legend: blue ($D = 0.43$ V/nm, $\Delta \sim 2.4$ meV); purple ($D = 0.48$ V/nm, $\Delta \sim 3.4$ meV; green ($D = 0.53$ V/nm, $\Delta \sim 3.2$ meV), cyan ($D = 0.58$ V/nm, $\Delta \sim 2.6$ meV); red ($D = 0.68$ V/nm, $\Delta \sim 1.4$ meV); yellow ($D = 0.76$ V/nm, $\Delta \sim 0.93$ meV).

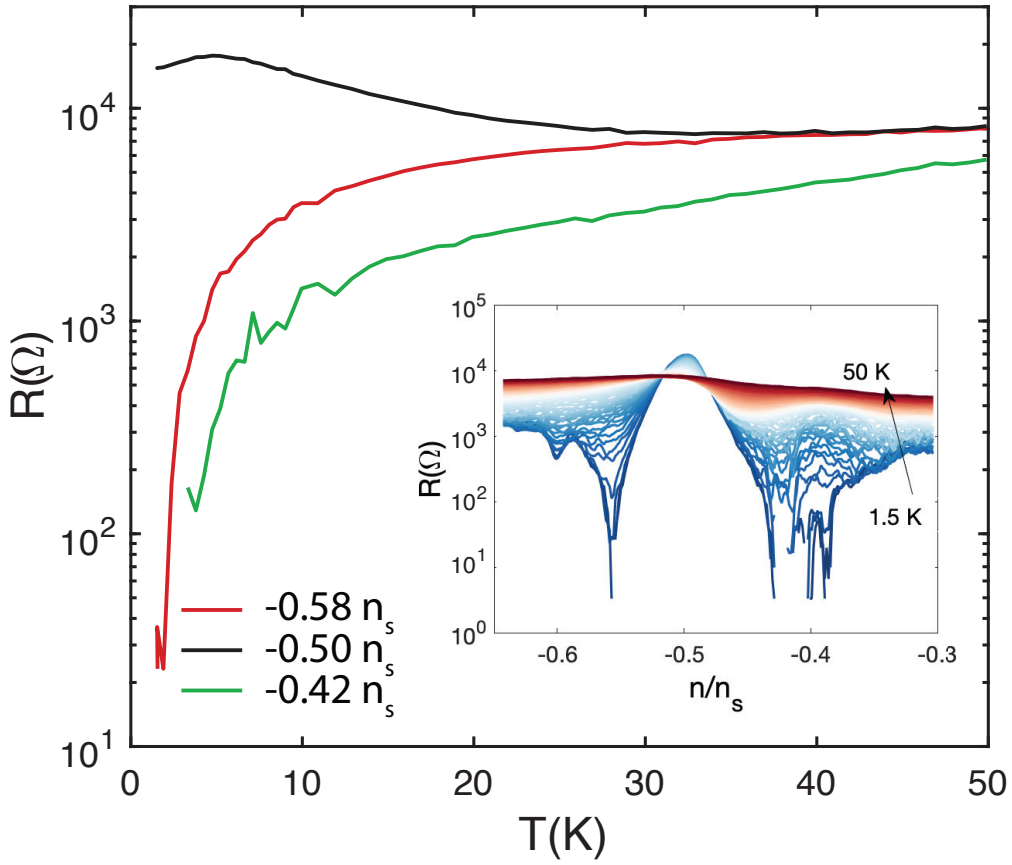

FIG. 16. **Onset of zero resistance in 5.1° sample.** Resistance versus temperature showing insulating behaviour at half-filling and two zero resistance pockets in the neighborhood of half-filling. Inset: resistance versus band-filling from 1.5K to 50K.

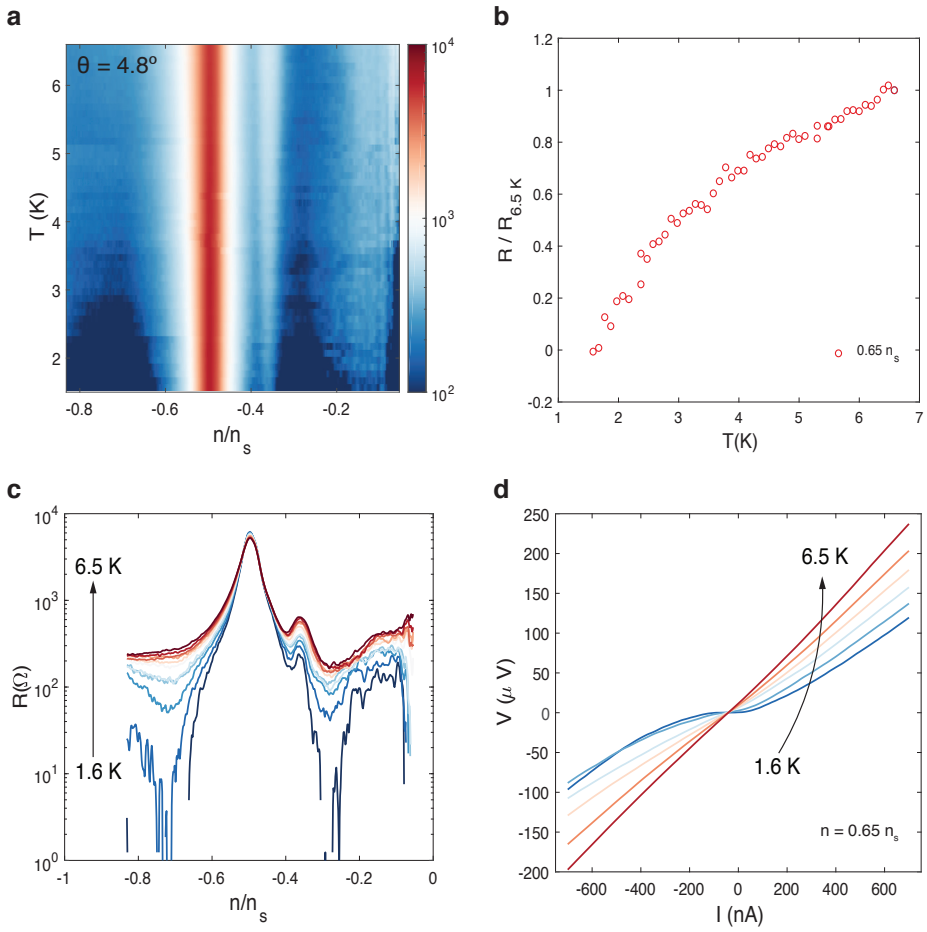

FIG. 17. **Onset of zero resistance in 4.8° sample.** Resistance map with temperature and filling fraction (**a**) and the corresponding line-cuts along different temperatures (**c**) show two zero resistance pockets flanking the insulator. **b,** R vs T shows zero resistance onsets below about 2K, similar to the behavior of 5.1° sample. **d,** The IV curve along one of the pocket at different temperatures, showing non-linearity below $T = 2$ K.

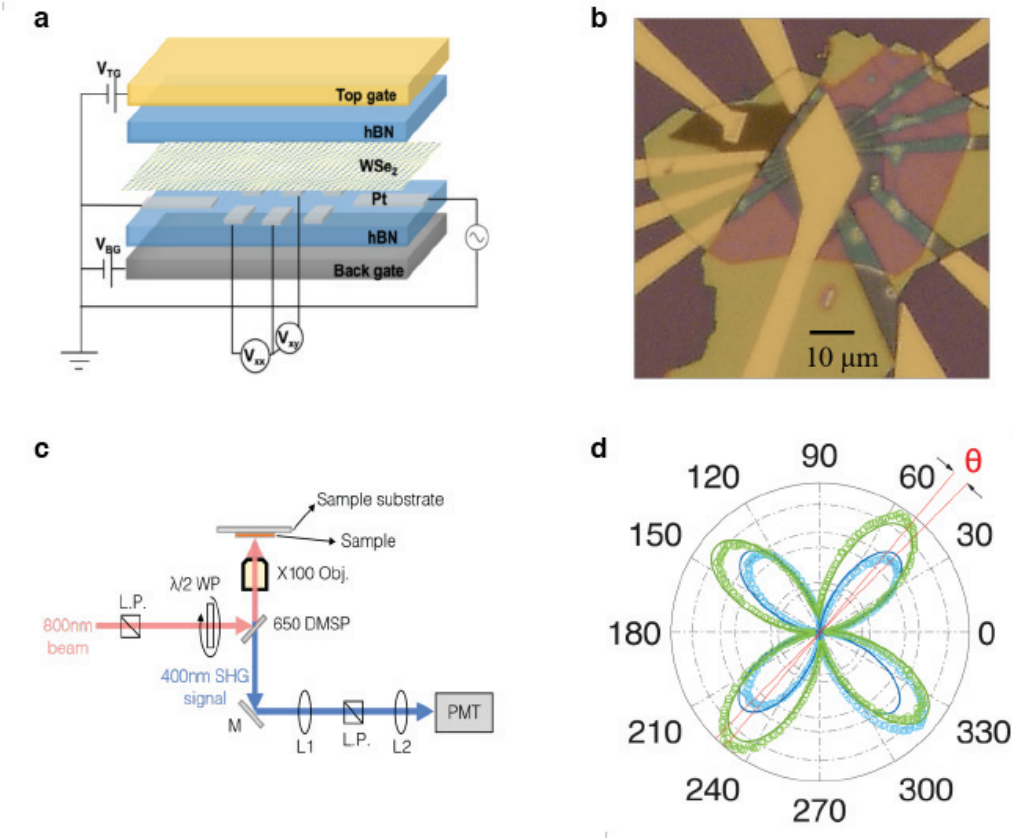

FIG. 18. **Device structure and characterization of twist angle from SHG. a,** Device and measurement schematics. **b,** Optical image of a device with bottom graphite gate and top metal gate. **c,** Second harmonic generation (SHG) setup. **d,** SHG data (dotted) and fit (solid) of WSe_2 monolayers twisted by a small angle.

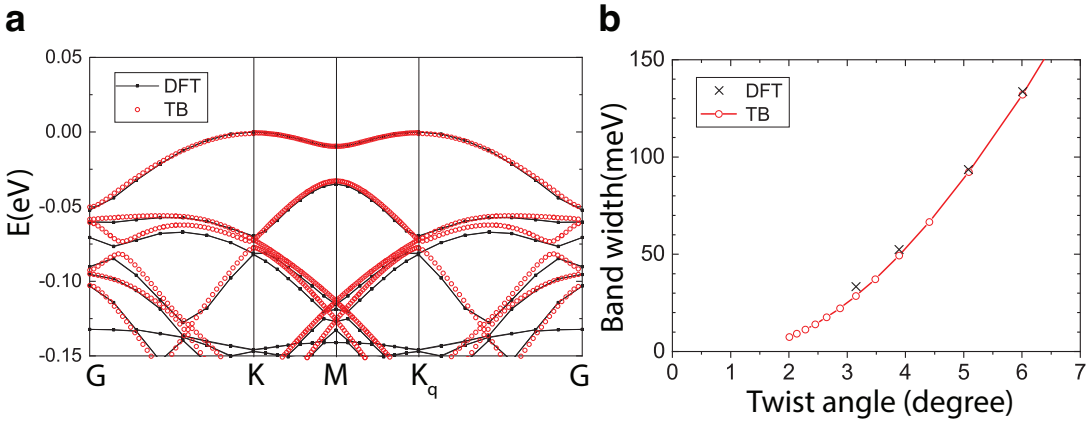

FIG. 19. **Comparison of the results calculated by TB model and calculations with DFT. a,** Band structures of twisted bilayer WSe_2 at 3.89° calculated by DFT (black solid lines) and TB model (red circles). **b,** Band width of the top of the valence bands at different twist angles calculated with DFT (black crosses) and TB model (red solid lines).